Toward Calculations of the ^{129}Xe Chemical Shift in Xe@C_{60} at Experimental Conditions: Relativity, Correlation, and Dynamics

Michal Straka,*,†,‡ Perttu Lantto,†,£,§ and Juha Vaara†,#

Laboratory of Physical Chemistry, Department of Chemistry, University of Helsinki, P.O. Box 55 (A. I. Virtasen aukio 1), FIN-00014 Helsinki, Finland, Institute of Organic Chemistry and Biochemistry, Academy of Sciences of the Czech Republic, Flemingovo n. 2., CZE-16610 Praha 6, Czech Republic, and NMR Research Group, Department of Physical Sciences, University of Oulu, P. O. Box 3000, FIN-90014 Oulu, Finland

Received: December 12, 2007; In Final Form: January 9, 2008

We calculate the ^{129}Xe chemical shift in endohedral Xe@C_{60} with systematic inclusion of the contributing physical effects to model the real experimental conditions. These are relativistic effects, electron correlation, the temperature-dependent dynamics, and solvent effects. The ultimate task is to obtain the right result for the right reason and to develop a physically justified methodological model for calculations and simulations of endohedral Xe fullerenes and other confined Xe systems. We use the smaller Xe···C_6H_6 model to calibrate density functional theory approaches against accurate correlated wave function methods. Relativistic effects as well as the coupling of relativity and electron correlation are evaluated using the leading-order Breit−Pauli perturbation theory. The dynamic effects are treated in two ways. In the first approximation, quantum dynamics of the Xe atom in a rigid cage takes advantage of the centrosymmetric potential for Xe within the thermally accessible distance range from the center of the cage. This reduces the problem of obtaining the solution of a diatomic rovibrational problem. In the second approach, first-principles classical molecular dynamics on the density functional potential energy hypersurface is used to produce the dynamical trajectory for the whole system, including the dynamic cage. Snapshots from the trajectory are used for calculations of the dynamic contribution to the absorption ^{129}Xe chemical shift. The calculated nonrelativistic Xe shift is found to be highly sensitive to the optimized molecular structure and to the choice of the exchange−correlation functional. Relativistic and dynamic effects are significant and represent each about 10% of the nonrelativistic static shift at the minimum structure. While the role of the Xe dynamics inside of the rigid cage is negligible, the cage dynamics turns out to be responsible for most of the dynamical correction to the ^{129}Xe shift. Solvent effects evaluated with a polarized continuum model are found to be very small.

1. Introduction

The Xe atom is an excellent nuclear magnetic resonance (NMR) probe. It is chemically very inert, and its NMR parameters sensitively respond to the surroundings of the Xe atom due to its large and polarizable electron cloud. Consequently, the Xe atom spans a substantial chemical shift range when dissolved in different solvents or materials and even a much larger range in xenon-containing molecules.[1] The sensitivity of the ^{129}Xe NMR parameters allows noninvasive studies of material properties and microscopic processes on the NMR time scale. There are numerous representative examples, for example, the studies of solvent dynamics in liquids,[2] orientational and translational order in liquid crystals,[3] the structure of micro- and mesoporous solids,[4] as well as structure of surfaces,[5] glasses,[6] and polymers.[7] Recent interest has also been focused on studies of biological materials such as proteins,[8] tissues,[9] and cells.[10]

Xenon NMR experiments provide useful information about material properties, but their interpretation at the microscopic level is not always straightforward. Computational science presents a powerful tool for tackling this problem.[11−20] The Xe guest−host systems still present a challenge to modeling due to the importance of the relativistic and electron correlation effects as well as the dynamic nature of these systems. A proper computational model of a confined Xe system should include all of the experimental conditions to provide physically well-based computational predictions of Xe NMR parameters. These are, in short, relativistic and correlation effects as well as their coupling, thermal effects due to molecular dynamics, and the effects of the environment, such as the solvent or matrix influences. Our interest is to combine the available computational approaches and include the above-mentioned mechanism into calculations to reproduce, as closely as possible, the experimental conditions.

This study concentrates on the isotropic ^{129}Xe chemical shift, δ(Xe), in endohedral Xe@C_{60} (Figure 1b). This system serves as a prototype for confined Xe species. It is a compact and highly symmetric molecule of I_h symmetry. We build an experiment-oriented computational model as outlined above and pursue insight into the relative importance of the different contributions.

Xe@C_{60} was first experimentally prepared by Syamala, Cross, and Saunders[21] by exposing C_{60} to Xe gas at 3000 atm at 650 K. The measured ^{129}Xe isotropic NMR chemical shift in

* To whom correspondence should be addressed. E-mail: straka@chem.helsinki.fi.
† University of Helsinki.
‡ Academy of Sciences of the Czech Republic.
£ University of Oulu.
§ E-mail: perttu.lantto@oulu.fi.
# E-mail: juha.t.vaara@helsinki.fi.

10.1021/jp711674y CCC: $40.75
Published on Web 02/28/2008

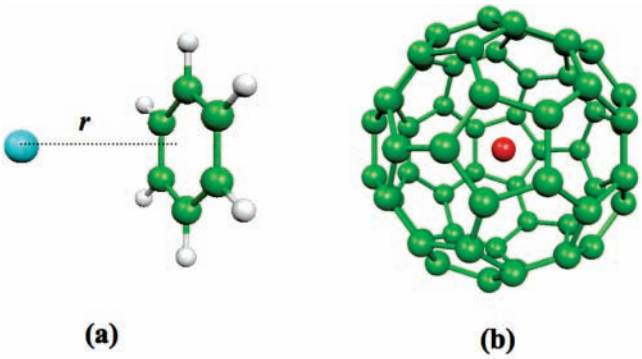

Figure 1. Structures of the presently studied Xe···C_6H_6 (a) and Xe@C_{60} (b) systems.

Xe@C_{60} dissolved in benzene was found at 179.2 ppm with respect to the Xe gas, which is 8.9 ppm smaller than the shift of atomic ^{129}Xe dissolved in benzene (188.1 ppm with respect to the Xe gas). The cage carbons in Xe@C_{60} are experimentally 0.95 ppm less shielded than those in the empty C_{60} cage.[21]

Several theoretical studies of the chemical shift of ^{129}Xe@C_{60} are found in the literature. Bühl, Patchkovskii, and Thiel[18] used the Hartree−Fock (HF) approach and obtained a low value of 71.7 ppm for the ^{129}Xe shift. Sears and Jameson[19] used nonrelativistic (NR) density functional theory (DFT) with the B3LYP functional in static equilibrium geometry calculations and obtained an excellent agreement with the experiment. Autschbach and Zurek in ref 20 used the zeroth-order relativistic approximation (ZORA) DFT approach in a careful investigation of the methodological aspects of the problem, including the basis set limit, choice of the exchange−correlation functional, role of the relativistic effects, and a rough estimate of the role of the dynamics of the Xe atom in the rigid cage. The results obtained in ref 20 span a broad range depending on the functional used, basis set, and underlying molecular structure. A general feature of the generalized gradient approximation (GGA) DFT functionals used is that the shifts are overestimated by tens of ppm as compared to the experimental result. At the same time, HF approximation clearly underestimates the ^{129}Xe shift[18] (vide supra). It is nevertheless evident from the ZORA results that relativistic effects play a non-negligible role as the inclusion of scalar relativistic effects was found to increase the shift by 17.5 ppm at the BP86 GGA level, and a further change of −1.9 ppm resulted from the spin−orbit (SO) effects. The importance of the relativistic effects indicates that the excellent agreement of the NR DFT results of ref 19 with the experiment is coincidental.

In this paper, we present a systematic investigation of the ^{129}Xe NMR chemical shift in Xe@C_{60}. We start with quantum chemical calculations of the system at rest, at its optimized equilibrium structure. Xe@C_{60} itself as well as the typical experimentally interesting systems with a confined Xe atom is too large to be treated by accurate ab initio wave function theories, and we are thus limited to the DFT methods. DFT has been found to perform well for the ^{129}Xe chemical shifts in weakly bonded systems where the induced shifts are dominated by overlap effects.[11,17,22,23] The DFT errors mainly occur in the NR contribution to the chemical shift, whereas the relativistic effects are fairly well approximated at the DFT level.[11,24,25] However, the results still depend on the choice of the functional, and thus, DFT has to be calibrated against more accurate methods. This we do using the smaller Xe···C_6H_6 system shown in Figure 1a. Calibration of DFT against ab initio methods up to CCSD(T) (coupled-cluster single, double, and noniterative triple substitutions) data for the NR part of the shielding allows for selecting a well-performing functional and converged basis set to be used in DFT calculations of the Xe@C_{60} system.

The relativistic effects on the ^{129}Xe chemical shift are treated using the recently developed Breit−Pauli perturbation theory (BPPT)[26,27] at the DFT level. This approach has been carefully tested,[11,24,25] and it has the advantage of enabling the estimation of the leading-order relativistic effects using both DFT and correlated ab initio methods. So far, BPPT is the only available method for the latter purpose. Hence, it enables systematic treatment of the coupling of electron correlation and relativity.

The influence of Xe atom dynamics inside of a fixed-geometry cage can be intuitively separated from the cage dynamics, as the cage is quite rigid and the dynamics of the heavier Xe atom is characterized by a much lower frequency than that of the cage carbons. We exploit the fact that the potential inside of the cage is, to a very good approximation, centrosymmetric. The solution is then mapped to the quantum mechanical rovibrational problem of a quasi-diatomic system in which C_{60} represents a quasi-atom. Classical molecular dynamics (MD) simulations are performed to relax the rigid cage assumption. We use first-principles Born−Oppenheimer (BO) MD, that is, the forces acting on the atoms are calculated on the fly from the (DFT) potential energy hypersurface. The obtained trajectories are used for snapshot calculations of the ^{129}Xe shift to obtain the thermal motion correction at the temperature of 300 K.

Finally, solvent effects are briefly discussed in terms of both the polarized continuum modes (PCM)[28] and explicit solvent molecules.

2. Computational Methods

2.1. Software. Turbomole 5.9.1 (ref 29), Gaussian 03 (ref 30), and the Mainz−Budapest−Austin version of ACES-II (ref 31) codes were employed in the NR calculations. The BPPT results were obtained with a locally modified version of Dalton.[32] Different parameters such as the convergence of the self-consistent procedure, accuracy of integrals, and the quality of integration grids in DFT calculations were carefully checked before the production calculations to avoid numerical noise. Default values were found sufficient for most of the parameters. The SCF energy gradient was tightened to 5×10^{-8} au in BPPT calculations.

2.2. Models. We calculated the Xe···C_6H_6 system (Figure 1a) at a sequence of NR levels with systematically improving accuracy and increasing computational cost: HF, second-order Møller−Plesset many-body perturbation theory (MP2), coupled-cluster singles and doubles (CCSD), as well as CCSD(T). We estimated the basis set limit at the less-demanding but correlated MP2 level. Ab initio results are compared to the DFT data using the basis set converged at the MP2 level. The best-performing functional (BHandHLYP,[33,34] vide infra) was selected for the production calculations of the Xe@C_{60} shifts, including the snapshots from the simulations. The best functional for the structure optimization (BP86,[35,36] vide infra) was used to generate the MD trajectory. For accurate calculations of the potential energy surface of Xe within the rigid cage, we used MP2 and the spin-component-scaled MP2 (SCS-MP2)[37] approach using the default parameters.

2.2.1. Molecular Structures. For Xe···C_6H_6 basis set convergence study, we used the minimum-energy structure obtained from a basis set superposition error (BSSE)-corrected optimization at the MP2/def2-TZVP level in Turbomole, with the benzene structure kept fixed at the geometry with r(C−C) =

1.406 and r(C−H) = 1.080 Å. The resulting Xe−ring center distance was 3.770 Å. In the calculated property curves, the Xe−C_6H_6 distance was varied from 2.8 to 5.0 Å.

No experimental structure has been reported for Xe@C_{60}. Calculations show that the C_{60} structure does not alter appreciably when Xe is inserted (vide infra). We thus used the experimentally reported gas-phase structure of C_{60} (ref 38) with two distinct C−C bonds, r(C═C) = 1.401 Å and r(C−C) = 1.458 Å. This corresponds to r(Xe−C) = 3.562 Å.

2.2.2. Exchange−Correlation Functionals. DFT results are reported with the following GGA functionals: BP86,[35,36] BLYP,[34,35] PBE,[39] as well as with the hybrid B3LYP,[33,35,41] B3P86,[33,35,36] B3PW91,[33,35,42] BHandHLYP,[33,35] B97-1,[43] PBE0,[57] TPSSH,[58] and KT3[44] functionals.

2.2.3. Basis Sets and Pseudopotentials in Non-BPPT Calculations. The split-valence basis sets implemented in Turbomole, def-SVP, def-TZVP, def-TZVPP, TZVPPP, def2-TZVPP, and def2-QZVP (ref 45), together with the corresponding auxiliary basis sets were employed in the resolution-of-the-identity MP2 (RI-MP2)[46] calculations. For structure and energy calculations, Xe valence basis sets were used with the corresponding quasirelativistic effective core potentials (ECP). The 8-VE (valence electron) ECP[47] was employed in combination with the older def- basis sets and the 26-VE ECP for the new def2- basis sets.[48] For NR calculations, we used the modified all-electron Xe basis set by Hanni et al.[13]

2.3. Relativistic Corrections to Shielding via Breit−Pauli Perturbation Theory. *2.3.1. Background.* In BPPT, relativistic effects are treated as perturbations on equal footing with the magnetic perturbation operators, acting on a nonrelativistic spin-free reference wave function.[26,27] When only one-electron, leading-order [$O(\alpha^4)$, where α is the fine-structure constant] contributions are included, 16 relativistic corrections are obtained on top of the NR shielding

$$\boldsymbol{\sigma}_{\mathrm{TOTAL}} = \boldsymbol{\sigma}_{\mathrm{NR}} + \boldsymbol{\sigma}_{\mathrm{BPPT}} \tag{1}$$

where

$$\begin{aligned}\boldsymbol{\sigma}_{\mathrm{BPPT}} = {} & \boldsymbol{\sigma}_{\mathrm{con}} + \boldsymbol{\sigma}_{\mathrm{dip}} + \boldsymbol{\sigma}_{\mathrm{d-KE}} + \boldsymbol{\sigma}_{\mathrm{p-OZ}} \\ & + \boldsymbol{\sigma}_{\mathrm{d/mv}} + \boldsymbol{\sigma}_{\mathrm{d/Dar}} + \boldsymbol{\sigma}_{\mathrm{p/OZ-KE}} + \boldsymbol{\sigma}_{\mathrm{p-KE/OZ}} \\ & + \boldsymbol{\sigma}_{\mathrm{FC-II}} + \boldsymbol{\sigma}_{\mathrm{SD-II}} + \boldsymbol{\sigma}_{\mathrm{FC/SZ-KE}} + \boldsymbol{\sigma}_{\mathrm{SD/SZ-KE}} \\ & + \boldsymbol{\sigma}_{\mathrm{p/mv}} + \boldsymbol{\sigma}_{\mathrm{p/Dar}} \\ & + \boldsymbol{\sigma}_{\mathrm{FC-I}} + \boldsymbol{\sigma}_{\mathrm{SD-I}}\end{aligned} \tag{2}$$

consists of expectation value terms (con to p-OZ), second-order terms via singlet (d/mv to p-KE/OZ) and triplet (FC-II to SD/SZ-KE) excited states, and third-order terms involving only singlet (p/mv and p/Dar) as well as both singlet and triplet (FC-I and SD-I) excited states. The BPPT contributions can be interpreted in terms of familiar NR concepts. The terms d+p/mv+Dar as well as FC-I and SD-I are "passive" relativistic contributions where the mass−velocity (mv), Darwin (Dar), and spin−orbit (SO, in the FC-I and SD-I terms) operators change the wave function on which the NR hyperfine and Zeeman operators act. In the remaining, "active" terms, the hyperfine and/or Zeeman operators themselves are relativistically modified. For a thorough derivation of the theory as well as specification of the contributing terms, we refer to the original papers.[26,27]

In the course of this work, it was found that besides the NR contribution, five relativistic terms in the BPPT expansion are responsible for the majority of the chemical shift and shielding anisotropy: p-KE/OZ, p/mv, p/Dar, FC-I, and SD-I. The other terms are practically chemically invariant, very nearly spherically symmetric core-type contributions. This seems to be a very general phenomenon for Xe systems.[11,24,25]

2.3.2. Basis Sets in BPPT. Relativistic contributions necessitate additional tight basis functions to describe the electron cloud close to the nuclei. For Xe, the requirements have been tested in our previous studies.[11,24,25] The uncontracted Faegri-IV[49] (FIV) basis supplemented with six high-exponent (tight) as well as one small-exponent (diffuse) spd sets resulted, in total, in 27s23p22d2f functions, which were found to provide convergence to within less than 0.5 ppm of the ^{129}Xe chemical shift and shielding anisotropy.[11,24,25] This basis set is denoted as FIVu61. For the light centers (C and H), the def-TZVP and def-TZVPP basis sets were tested. Common-gauge origin (CGO) was placed at the Xe atom in the BPPT calculations.

2.3.3. Correlation Treatment in BPPT. As shown in the previous studies of Xe_2[11] and HXeCCH,[25] DFT may be used with fair accuracy to approximate the ab initio BPPT approach, which is, in turn, not accessible for the large Xe@C_{60}. The BLYP (0% exact-exchange admixture), B3LYP (20%), and BHandHLYP (50%) functionals were used for the BPPT contributions.

2.4. Xe Dynamics in the Cage. The potential experienced by the Xe atom in a rigid I_h-symmetric C_{60} cage is centrosymmetric (vide infra). This reduces the rovibrational problem to that of a diatomic molecule with Xe and C_{60} constituting the "atoms". The solution was obtained numerically using the VIBROT code written by Sundholm,[50] which calculates rovibrationally averaged properties for a diatomic system from the potential energy and property curves as functions of the interatomic distance. In our quasi-diatomic Xe@C_{60}, the "interatomic" potential is represented by counterpoise-corrected SCS-MP2 energy calculated for Xe@C_{60} with the Xe atom displaced from the center. Six equidistant points with Xe displaced by 0.0−0.5 Å in five distinct symmetry directions from the cage center were calculated to map the potential and the property curves. These symmetry directions ran from the center of the cage toward a carbon atom, the center of a pentagon, the center of a hexagon, the midpoint of a bond connecting two hexagons, and the midpoint of a bond connecting a hexagon with a pentagon. In VIBROT calculations, the potential and property curves were fitted to fourth-order polynomials. The numerical parameters in VIBROT were carefully tested to ensure convergence. The results presented below were produced with the maximum vibrational and rotational quantum numbers set to $\nu = 6$ and $J = 200$. This produced convergence to within 0.01 ppm for the average shift at all of the calculated temperatures.

2.5. Molecular Dynamics of Xe@C_{60}. First-principles BO molecular dynamics was employed, where atom cores move as classical particles on the electronic energy hypersurface, calculated quantum chemically on the fly. This was done using the Frog module of the Turbomole code,[29] with the Leapfrog−Verlet algorithm.[51] The RI-BP86/SVP level was used for the electronic energy and gradients. Special attention had to be paid to the precision of the wave function and forces; hence, the default convergence thresholds for both were tightened to 10^{-8} au. The numerical DFT grid "m5" of Turbomole was used. The calculations were carried out in the microcanonical (NVE) ensemble. In each separate simulation, the initial kinetic energy of the Xe atom was chosen to correspond to the instantaneous temperature of 300 K, while the direction of the initial velocity

was selected randomly. The carbon velocities were sampled from the Maxwell−Boltzmann distribution at 300 K.

As was observed in preliminary tests at 300 K, the time step of 160 au (ca. 4 fs) gives stable dynamics where the system equilibrates very fast. The dynamics of the system is characterized by relatively small coupling between the Xe atom and the cage. Indeed, in a rigid cage, the guest atom would adopt an orbiting trajectory[52] which only covers a limited part of the available phase space. In a dynamic cage, the sampling efficiency is somewhat enhanced, but to ensure adequate sampling of the configuration space over a manageable total simulation time, we performed a number of short time simulations instead of a single long one. All in all, 20 simulations, each of 256 steps length (about 1 ps), were done. Hence, the equivalent of a nearly 20 ps trajectory was sampled.

The instantaneous snapshots of the trajectories were selected in the following way. After the very rapid equilibration in about 30 steps (ca. 120 fs), we selected 5 snapshots from each simulation, using equidistant intervals of 45 steps. The estimate of statistical errors was obtained by the "blocking" method described by Flyvbjerg and Petersen.[53] The method involves consecutive halving of the amount of data, where at each step, two adjacent data points are averaged to give a new data point for the next round, producing a half as large data set. The statistical correlation contained in the data decreases with the number n of the transformations, and consequently, error estimates are improved in the process. The proper error bar is selected from the plateau observed as a function of n.

2.6. Solvent Effects. Solvent effects were calculated using the self-consistent reaction field model implemented in Gaussian 03, namely, the conductor-like polarized continuum model (CPCM).[28] Tests were also made with explicit solvent molecules as described in the Results and Discussion section below.

2.7. Additional Details. The chemical shifts δ were calculated using the free Xe atom and CH_4 [r(CH) = 109.4 pm] as reference systems for ^{129}Xe and ^{13}C, respectively, according to

$$\delta = (\sigma_{ref} - \sigma)/(1 - \sigma_{ref}) \quad (3)$$

where σ and σ_{ref} are the calculated shielding constants in Xe@C_{60} or Xe···C_6H_6 and in the reference system, respectively. We also report shielding anisotropies

$$\Delta\sigma = \sigma_{||} - \sigma_{\perp} \quad (4)$$

in Xe...C_6H_6, where $\sigma_{||}$ and $\sigma_{\perp}$ are the respective components of the shielding tensor along with and perpendicular to the 6-fold symmetry axis of Xe...C_6H_6. The ^{131}Xe nuclear quadrupole coupling in Xe...C_6H_6 is also reported for future reference. In the NQCC calculations we used the nuclear quadrupole moment $Q(^{131}\text{Xe}) = -114$ mb (ref 54).

3. Results and Discussion

3.1. Calibration of DFT for Xe···C_6H_6. *3.1.1. Basis Set Limit at the Nonrelativistic MP2 Level.* We start by probing the basis set convergence of the ^{129}Xe shift and ^{131}Xe quadrupole coupling in Xe···C_6H_6 at the lowest correlated ab initio level, MP2, which is used for three reasons: (a) Even for the small Xe···C_6H_6 system, it is hard to search for the basis set limit with accurate CC approaches, (b) the basis set convergence at the MP2 level should nevertheless mimic the CC one, and (c) both the DFT and HF methods are expected to converge faster toward the basis set limit than MP2, rendering the basis set for which converged MP2 results are obtained automatically sufficient also for DFT and HF.

TABLE 1: Basis Set Effects on $^{129/131}$Xe Nuclear Magnetic Resonance Properties in Xe···C_6H_6 (at r = 3.77 Å) Calculated at the Nonrelativistic MP2 Level

basis Xe	basis C,H	δ(Xe)/ppm	$\Delta\sigma$(Xe)/ppm	NQCC(Xe)/MHz
FII+3s2p2d1f	def-TZVP	−14.9	16.8	4.559
FII+3s2p2d1f[a]	def-TZVP	−14.9	16.7	4.544
FII+3s2p2d2f[b]	def-TZVP	−14.7	16.5	4.453
FII+3s2p2d3f[c]	def-TZVP	−14.6	16.5	4.466
FII+3s2p2d3f1g[d]	def-TZVP	−14.4	16.4	4.351
FII+2s1p1d1f	def-TZVP	−15.0	17.0	4.574
FII+2s1p1d2f	def-TZVP	−14.7	16.6	4.600
FII+3s2p2d1f	def-SVP	−13.2	16.1	4.927
FII+3s2p2d1f	def-TZVPP	−14.6	16.7	4.359
FII+3s2p2d1f	def-TZVPPP	−14.6	15.7	4.208
FII+3s2p2d1f	def2-QZVP	−14.3	16.6	4.142

[a] Decontracted. [b] The exponents of the f primitives: α_f = 0.377587, 0.125862. [c] α_f = 0.654, 0.218, and 0.0727. [d] α_g = 0.545.

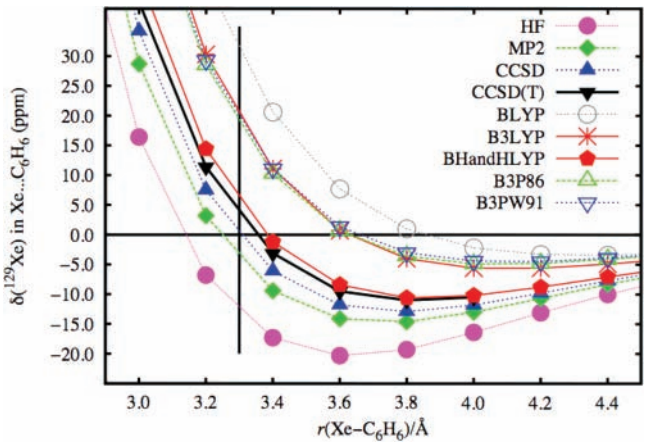

Figure 2. ^{129}Xe chemical shift in the Xe···C_6H_6 model, calculated at different levels as a function of the Xe−C_6H_6 distance, r, indicated in Figure 1. The MHA-TZVP basis set was used (see text). The vertical line indicates the Xe to the center of the C6 ring distance in Xe@C_{60}.

Table 1 shows the basis set dependence of the ^{129}Xe chemical shift, δ(Xe), the shielding anisotropy, $\Delta\sigma$(Xe), and the ^{131}Xe nuclear quadrupole coupling constant, NQCC(Xe), in Xe···C_6H_6. The corresponding data calculated with HF (without NQCC) are provided in Table S1 in the Supporting Information. The optimized FII+3s2p2d1f Xe basis set by Hanni et al.[13] is converged well within 1 ppm for both δ(Xe) and $\Delta\sigma$(Xe). Additional tight, diffuse, or polarization functions do not appreciably change the results. We can actually afford removing the most diffuse spd set from Hanni's basis without loss of accuracy. A larger effect is observed when an f function is added. The results depend only negligibly on the benzene basis set. TZVP on C/H already gives results converged to within 1 ppm. The ^{131}Xe NQCC converges also very fast. Thus, in the production calculations of Xe···C_6H_6, we can use Hanni's basis set for Xe (FII+3s2p2d1f), with the most diffuse spd set removed and equipped with an additional f function, resulting in a contracted [22s17p14d2f/15s13s11d2f] basis. TZVP basis sets are employed for C and H. We will refer to this combination as MHA-TZVP.

3.1.2. Nonrelativistic NMR Properties and Energetics in Xe···C_6H_6. ^{129}Xe Isotropic Chemical Shift and Shielding Anisotropy. Using the converged (in the MP2 sense) basis set, we can now compare the performance of DFT and correlated ab initio methods. Of numerous existing exchange−correlation functionals, we are limited to those for which the second derivatives are accessible in the available codes. Figure 2 shows the dependence of the calculated δ(Xe) on the Xe−C_6H_6

distance. Numerical data including results for additional functionals not plotted in Figure 2 (B97-1, B98, PBE, PBE0, KT3) are provided in Table S2 in the Supporting Information. Using CCSD(T) as a benchmark in Figure 2, we observe that upon elongation of the Xe−C_6H_6 distance, the δ(Xe) first rapidly decreases, reaches a minimum near the equilibrium geometry (around 3.8 Å), and then gradually converges toward zero at infinity. The HF approximation substantially exaggerates the negative δ(Xe) in the intermediate distance range but reproduces the qualitative trends of the CCSD(T) curve. Thus, in the qualitative sense, it outperforms the pure (nonhybrid) density functionals, which only give a very shallow minimum at long distances (Table S2, Supporting Information). Inclusion of electron correlation via the ab initio MP2 and CCSD methods increases δ(Xe) and flattens the curve toward the best CCSD(T) results. Interestingly, the zigzag trend (vide infra), often observed for energetics in the HF, MP2, CCSD, CCSD(T) series of methods, is not seen in the δ(Xe) curves in Figure 2. Instead, upon improving the level from HF through MP2 and CCSD toward CCSD(T), the shift becomes monotonically more positive. In Xe_2, the zigzag trend persists.[11]

The GGA functionals, such as BLYP in Figure 2 or the very similar B98 and PBE (Table S2), give rather poor results. They overshoot δ(Xe) and do not even reproduce the qualitative trends, particularly the position of the minimum on the curve. The situation improves with hybrid functionals. A proper amount of exact-exchange admixture in the functional renders the results toward the CCSD(T) benchmark, as observed along the BLYP, B3LYP, and BHandHLYP series. The role of the correlation functional is less crucial; the B3LYP, B3PW91, and B3P86 curves in Figure 2 are almost identical. The BHandHLYP functional gives results closest to the currently most accurate CCSD(T) data and is the best candidate for production calculations of Xe@C_{60}.

Our BLYP results in Figure 2 for δ(Xe) are similar to those obtained by Bagno and Saielli who calculated δ(Xe) in Xe···C_6H_6 using the relativistic ZORA approach at the BP86/TZ2P level. Notice, however, that the GGA functionals seem to present the worst choice for calculating the NR Xe shift in Xe···C_6H_6 and, hence, are also dubious for the relativistic contributions.

The Xe−C_6H_6 distance near 3.3 Å, indicated by a vertical line in Figure 2, corresponds to the situation in Xe@C_{60}. Around this point, the dependence of the shift on the distance is very steep. Furthermore, some methods cross the zero shift level in this neighborhood. Our most accurate CCSD(T) calculations give a positive δ(Xe) of about +5 ppm at this distance, exaggerated by the best present DFT functional, BHandHLYP, by a couple of ppm. Depending on the method, anything between +30 and −15 ppm can be obtained for NR δ(Xe) at this distance. We can thus expect a very complicated situation in Xe@C_{60}.

The results for the shielding anisotropy $\Delta\sigma(^{129}Xe)$ in Xe··· C_6H_6, acquired in a similar manner as the Xe shifts in Figure 2, closely resemble the trends in Figure 2. The details on $\Delta\sigma$(Xe) in Xe···C_6H_6 are given for future reference in the Supporting Information, Table S3.

Nuclear Quadrupole Coupling. Figure 3 shows NQCC(Xe) versus the Xe−C_6H_6 distance calculated at different computational levels. The numerical data are given in Table S4 in the Supporting Information. No minimum is observed on the NQCC curves; the ^{131}Xe NQCC decreases monotonically with the Xe−C_6H_6 distance. The method dependence for NQCC is different from that of the Xe shift. The characteristic zigzag behavior

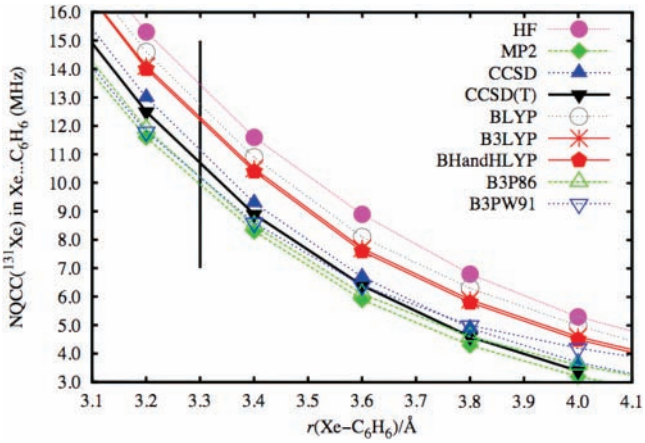

Figure 3. ^{131}Xe nuclear quadrupole coupling in Xe···C_6H_6, calculated at different levels as a function of the Xe−C_6H_6 distance, r, indicated in Figure 1. The MHA-TZVP basis set was used (see text). The vertical line indicates the Xe to the center of the C6 ring distance in Xe@C_{60}.

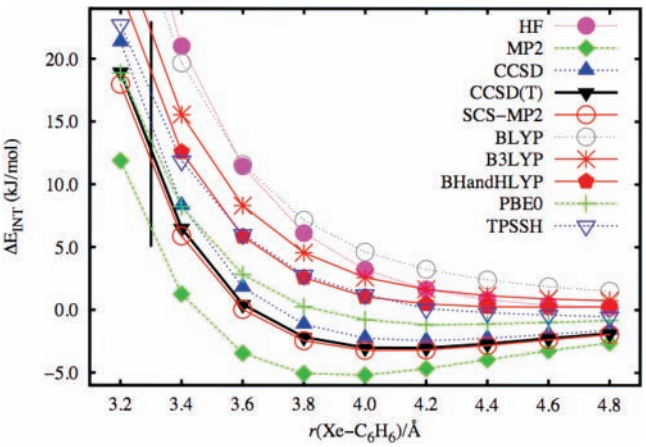

Figure 4. Interaction energy of the Xe···C_6H_6 complex, calculated at different levels as a function of the Xe−C_6H_6 distance, r, indicated in Figure 1. The def-TZVP basis set was used. The vertical line indicates the Xe to the center of the C6 ring distance in Xe@C_{60}.

along the series of ab initio correlation methods [HF, MP2, CCSD, CCSD(T)] is observed here. This behavior is characterized by MP2 providing an exaggerated correlation correction to the results, after which the CCSD data deviate again toward the HF results. Finally, CCSD(T) settles the issue at around two-thirds of the difference of the HF and MP2 data, closer to the latter. Typically, NQCC shows good convergence with respect to improving the correlation treatment. Presently, the CCSD(T) results are converged at least to within 0.5 MHz. Unlike the trends for δ(Xe) (Figure 2) and $\Delta\sigma$(Xe) (Table S3), the NQCC is not sensitive to the exact-exchange admixture in the functional but rather depends on the correlation functional, as seen from comparison of B3LYP, B3PW91, and B3P86 results in Figure 3. The different functional dependence is not surprising as NQCC is a first-order property computed as an expectation value of the ground-state wave function, whereas the NR nuclear shielding is a second-order property. In particular, the chemical shift arises mainly due to the paramagnetic shielding that originates in the coupling between the ground state and singlet excited states. B3PW91 and B3P86 perform best among the functionals tried; BHandHLYP systematically overestimates NQCC by a couple of MHz.

Energetics in Weak Bonding. Figure 4 compares the BSSE-corrected interaction energies for the formation reaction Xe + C_6H_6 = Xe···C_6H_6. The numerical data and results for further functionals are given in Table S5 in the Supporting Information.

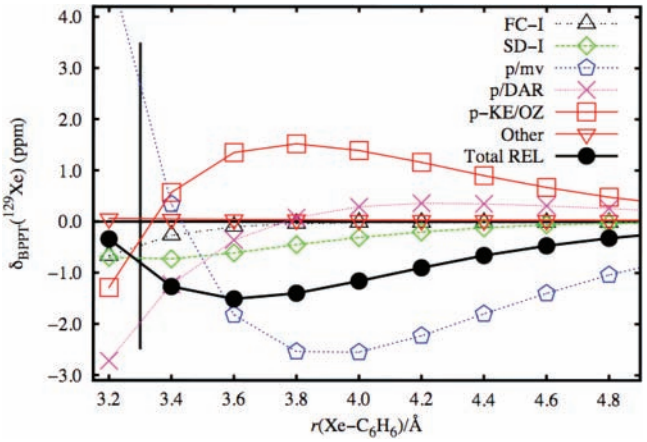

Figure 5. Five most important relativistic BPPT contributions to the ^{129}Xe chemical shift in the Xe···C_6H_6 complex, as functions of the Xe−C_6H_6 distance, r, indicated in Figure 1. "Other" stands for the sum of the other BPPT contributions. The BHandHLYP functional with the FIVu61/def-TZVP basis set was used for Xe/C and H. The vertical line indicates the Xe to the center of the C6 ring distance in Xe@C_{60}.

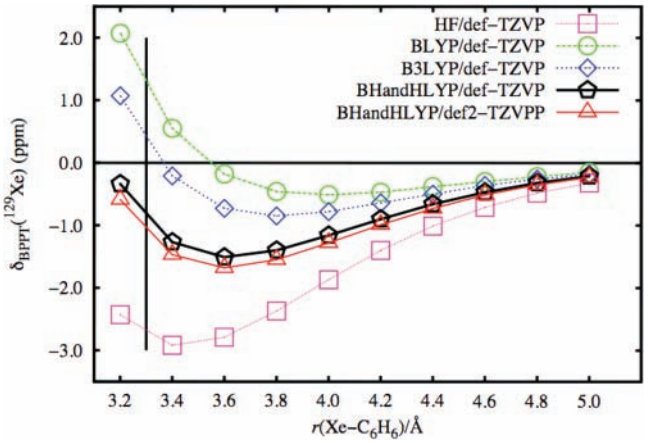

Figure 6. Results at different DFT levels for the total BPPT contribution to the ^{129}Xe chemical shift in the Xe···C_6H_6 complex as a function of the Xe−C_6H_6 distance, r, indicated in Figure 1. The basis sets for C and H are indicated. The FIVu61 basis set was used for Xe (see text). The vertical line indicates the Xe to the center of the C6 ring distance in Xe@C_{60}.

Note that for the energetics, scalar relativistic corrections are automatically included via the pseudopotentials used. Here, the appropriate valence basis set[48] is used along with the corresponding pseudopotential[47] for Xe instead of the all-electron basis set. The trends in the performance of the different methods are substantially different from those for the NR NMR properties. The convergence behavior with respect to the ab initio correlation treatment is similar to that of NQCC, that is, the zigzag pattern is observed. The tested DFT functionals and HF fail to describe the minimum of the potential curve. PBE0 provides results closest to the CCSD(T) data. Roughly speaking, it underestimates the interaction energy by the same amount as that by which MP2 overestimates it. The spin-component-scaled MP2 (SCS-MP2) approach provides results of very nearly CCSD(T) accuracy and is the best candidate for production work. We postpone the discussion of the basis set effects on energetics to be presented below in connection with Xe@C_{60}.

Summary of DFT Performance. BHandHLYP performs best for the ^{129}Xe chemical shift and the shielding anisotropy and will be used in the production calculations of Xe@C_{60}. Notably, it has been found to perform the best among the tested DFT functionals also for the ^{3}He shift in endohedral helium fullerenes[23] and for the ^{129}Xe shift in HXeCCH,[25] xenon fluorides,[24] as well as Xe_2 (ref 11). The satisfactory performance of BHandHLYP appears to be a very general observation for these properties. For NQCC(Xe), BHandHLYP overestimates the results, and the best data are obtained with B3PW91, B3P86, and PBE functionals. The DFT energetics should not be trusted for the Xe···C_6H_6 system. Instead, SCS-MP2 gives much better performance than MP2, with results very close to the CCSD(T) data. Note that the bonding situation is rather different in the Xe@C_{60} system, where the Xe atom is confined at a repulsive distance with respect to the aromatic rings. The interaction of the Xe atom with the cage is nevertheless found to be attractive.[55]

3.2. BPPT Relativity in Xe···C_6H_6. The BPPT relativistic corrections to the Xe chemical shift can be evaluated at HF, DFT, or ab initio CC and multiconfiguration self-consistent field levels. Ab initio BPPT would be, however, extremely demanding even for the smaller Xe···C_6H_6 model. We limit ourselves to the HF and DFT levels for Xe···C_6H_6, based on the previous experience from ab initio and DFT BPPT calculations in Xe systems.[11,24,25]

TABLE 2: Most Important Relativistic (BPPT) Contributions[a,b] to the ^{129}Xe Chemical Shift in Xe···C_6H_6 (at r = 3.8 Å); in ppm

BPPT term	HF	BLYP	B3LYP	BHandHLYP	BHandHLYP[c]
FC-I	−0.1	−0.2	−0.1	0.0	0.0
SD-I	−0.6	−0.3	−0.4	−0.5	−0.5
p/mv	−5.0	0.7	−0.7	−2.5	−2.9
p/Dar	0.6	−0.7	−0.3	0.1	0.1
p-KE/OZ	2.7	−0.1	0.6	1.5	1.7
BPPT-ALL	−2.4	−0.5	−0.9	−1.4	−1.6

[a] FIVu61 basis on Xe; def-TZVP on C. [b] The sum of the remaining contributions is below 0.1 ppm. [c] The def-TZVPP basis set on C.

Figure 5 shows the five most important BPPT contributions to δ(Xe) in Xe···C_6H_6. These are the p/Dar, p/mv, p-KE/OZ, FC-I, and SD-I terms. The remaining terms, referred to as "Other" in Figure 5, give a negligible total contribution to δ(Xe). They are both small in absolute value and also partially cancel out. This is in agreement with previous observations.[11,24,25] All BPPT terms vanish at long Xe···C_6H_6 distances. Notice that the p/Dar, p/mv, and p-KE/OZ terms are strongly distance-dependent. The FC-I and SD-I give small negative contributions, which increase in absolute value toward shorter distances.

Figure 6 shows the total BPPT correction δ_{BPPT}(Xe) to the ^{129}Xe shift in Xe···C_6H_6 calculated at HF and different DFT levels, as well as by using two different basis sets for benzene. Table 2 shows details about the particular contributions from the five main BPPT terms near the Xe−C_6H_6 minimum distance (3.8 Å). The numerical data are provided in the Supporting Information, Table S6. The remaining basis set effects beyond the def-TZVP level for C_6H_6 are of marginal importance for the description of the BPPT contribution to δ(Xe) in this system (Figure 6). Comparison of the results presented in Figures 2 and 6 shows that relativistic δ_{BPPT}(Xe) represents ∼10−15% of the nonrelativistic δ_{NR}(Xe) value. The BPPT proportion is largest at a quite short Xe−C_6H_6 distance range (3.4−3.8 Å), around the equilibrium distance in both Xe···C_6H_6 and Xe@C_{60}. The relativistic influence decreases at a larger separation. δ_{BPPT}(Xe) in Figure 6 behaves qualitatively similarly to δ_{NR}(Xe) in Figure 2, as a function of r. The position of the minimum and the well depth depend on the method in a manner similar to the NR case. HF gives the lowest values with the deepest minimum; DFT correlation makes the shift more

TABLE 3: Calculated Structures[a] of Xe@C_{60} and C_{60}; in Å

		Xe@C_{60}			C_{60}[b]	
method	basis set	r(Xe−C)	r_1(C−C)	r_2(C−C)	r_1(C−C)	r_2(C−C)
MP2	def-SVP	3.557	1.412	1.449	1.410	1.449
	def-TZVP	3.546	1.406	1.445	1.405	1.445
	def-TZVPP	3.542	1.405	1.443	1.404	1.443
	def2-TZVPP	3.541	1.405	1.443	1.404	1.443
BP86	def-SVP	3.574	1.409	1.461	1.408	1.459
	def-TZVP	3.560	1.401	1.456	1.400	1.455
	def-TZVPP	3.557	1.400	1.455	1.399	1.454
	def2-TZVPP	3.557	1.401	1.455	1.400	1.456
HF	def-TZVP				1.369	1.448
BLYP	def-TZVP				1.403	1.460
B3LYP	def-TZVP				1.390	1.451
BHLYP	def-TZVP				1.376	1.442
PBE	def-TZVP				1.399	1.454
PBE0	def-TZVP				1.386	1.445
TPSS	def-TZVP				1.398	1.453
TPSSH	def-TZVP				1.392	1.449
exp.[c]		3.562[d]			1.401	1.458

[a] Two unique C−C distances are sufficient to define the I_h C_{60} geometry. [b] The values in the lower part of the table (from HF onward) are adopted from ref 23. [c] Ref 38. [d] Distance from the center of the cage.

positive and flattens the curve. Increasing the exact-exchange admixture in the functional again deepens the shift minimum.

The situation where a negative total chemical shift is obtained at the energetically attractive distance range of the present Xe···C_6H_6 model, while the measured chemical shift of Xe in benzene solution is positive, is not self-contradictory. Whereas placing the Xe atom on the 6-fold axis of C_6H_6 is a good model for validating methods for the Xe@C_{60} case, such a coordination of the Xe and C_6H_6 subunits is much less relevant in the liquid. Due to many-body and thermal effects, large and positive shift contributions upon deep collisions of the Xe atom and solvent molecules in all possible on- and off-axis configurations dominate in solution.

3.3. Xe@C_{60} Calculations. *3.3.1. Static Results.* Molecular Structure. Results of geometry optimizations of Xe@C_{60}, presented in Table 3, suggest that the presence of the Xe atom in the center of the cage has almost no effect on the geometry of the C_{60} cage. The changes lie inside of the margins of numerical accuracy of the calculation at both the MP2 and the BP86 DFT levels used. We thus choose to use the experimentally known structure of gas-phase C_{60} for the calculations of Xe@C_{60}.

Despite having a weakly bonded complex, the GGA density functionals outperform the MP2 approach for the equilibrium structure because the inclusion of a weakly interacting spherical guest has no influence on the cage structure, which, in turn, is better calculated by GGA functionals. The hybrid and meta-GGA functionals actually give worse structures for the empty C_{60} than the pure GGA DFT. This has also been observed in our study of He@C_{60} (ref 23), from which some results are adopted into Table 3. The basis set effects are modest; the molecular structure of C_{60} is well-converged (within 0.001 Å) using the def-TZVP basis set.

Nonrelativistic ^{129}Xe Shift in Xe@C_{60}. Table 4 lists results for δ_{NR}(Xe) in Xe@C_{60} using different geometries and computational levels. The data reveals a critical sensitivity of the cage-induced ^{129}Xe shift to the cage structure. For example, the difference of about 0.019 Å in the Xe−C distance between the RIMP2/def-TZVPP and BP86/def-TZVP structures corresponds to 15−20 ppm in δ_{NR}(Xe). The BP86/def-TZVP structure corresponds to results very similar to those obtained at the experimental structure of the empty cage, yet a change of 0.002 Å in the Xe−C distance is enough to induce a shift change of

TABLE 4: Calculated Nonrelativistic ^{129}Xe Chemical Shift (in ppm) in Xe@C_{60} for Structures Optimized at Different Levels[a]

	structure optimization		
shift method	MP2/TZVPP	BP86/TZVP	exp. for C_{60}
HF[b]	68.0	59.6	59.1
BP86[c]	251.4	234.1	231.7
BLYP	239.2	222.5	220.3
B3LYP[d]	194.9	180.6	178.3
BHandHLYP	139.4	126.6	126.6
MP2	−	119.0	−
exp.			179.2
Xe−C distance (Å)	3.541	3.560	3.562

[a] Using the MHA basis for Xe and def-TZVP for C. [b] 71.7 ppm (ref 18). [c] 229.1 ppm (ref 20). [d] 181.6 ppm (ref 19).

TABLE 5: Nonrelativistic[a] ^{129}Xe Chemical Shift in Xe@C_{60} as Well as Relativistic BPPT Corrections Thereto[b] at the Experimental Structure of C_{60}; in ppm

contribution	BLYP	B3LYP	BHandHLYP
nonrelativistic	220.3	178.3	126.6
FC-I	−0.2	0.3	0.7
SD-I	1.4	1.2	0.9
p/mv	62.0	52.3	39.2
p/Dar	−12.9	−10.8	−8.0
p-KE/OZ	−31.3	−26.5	−20.1
BPPT(5)[c]	19.1	16.4	12.8
BPPT-ALL[d]	18.6	16.6	13.2
total[e]	238.9	194.9	139.8

[a] Using the MHA basis set on Xe and the def-TZVP basis set on C. [b] Using the FIVu61 basis set on Xe and def-TZVP on C. [c] Sum of the five most important contributions. [d] Sum of all BPPT contributions. [e] Sum of the nonrelativistic and BPPT-ALL contributions.

a couple of ppm. The significant sensitivity of δ(Xe) to the cage structure suggests a non-negligible dynamical contribution to δ(Xe) (vide infra).

The Xe shift in Xe···C_6H_6 is negative around the minimum distance, while it is positive in Xe@C_{60} with most of the presently considered approaches. The dependence of the calculated δ(Xe) on the exchange−correlation functional is a very critical one. Inspection of the last column in Table 4 reveals that the HF method gives a very low Xe shift of 59 ppm and the MP2 correlation increases the result to 119 ppm, still well below the experimental datum. The underestimation by the HF approach has been observed before by Bühl et al. (ref 18) as well as by Autschbach and Zurek (ref 20). The pure density functionals BLYP and BP86 give, in turn, very large values of 220 and 231 ppm, in agreement with ref 20. The shift decreases with increasing exact-exchange admixture in the functional, along the BLYP (231 ppm), B3LYP (179 ppm) and BHandHLYP (127 ppm) series. The B3LYP functional is closest to the experimental value of 179.2 ppm, but this can be considered as a "lucky strike", given the importance of dynamic and relativistic effects discussed below. If the BHandHLYP functional should be the best option as implied by the successful calibration on the Xe···C_6H_6 model (above) and also by our previous Xe NMR studies,[11,24,25] then our best static NR value for δ(Xe) of 126.6 ppm is still about 53 ppm below the experimental value. Can we recover the missing ∼50 ppm by the relativistic, dynamic, and solvent effects?

Relativistic BPPT Corrections. Table 5 lists the five most important relativistic BPPT corrections to δ(Xe) in Xe@C_{60}, together with the total BPPT contribution. Detailed BPPT data can be found in the Supporting Information, Table S7. In Xe@C_{60}, the relativistic shift contribution is positive, unlike that in Xe···C_6H_6 at the distance corresponding to the Xe−C

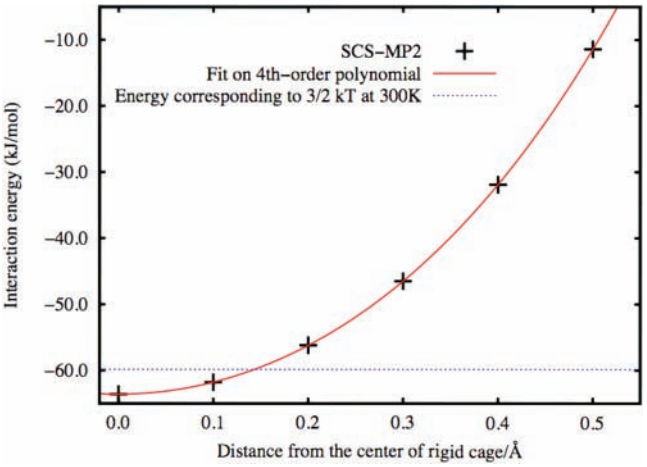

Figure 7. SCS-MP2/def2-TZVPP potential energy for the displacement of the endohedral Xe atom from the center of C_{60} along the five different symmetry directions toward the cage wall. Due to the very centrosymmetric potential, the results for all of the directions fall onto the same line. The cage is kept rigid.

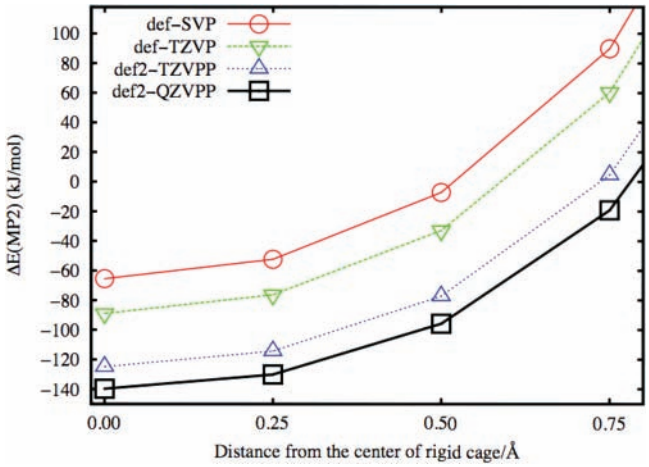

Figure 8. Basis set dependence of the calculated potential energy for displacement of Xe from the center of the C_{60} cage along different directions toward the cage wall in Xe@C_{60}. The cage is kept rigid.

distance in Xe@C_{60} (Figure 6). However, at very short Xe−C_6H_6 distances, the BPPT effect becomes positive due to the p/mv contribution, which is also responsible for the overall positive relativistic effect in Xe@C_{60}. Clearly, the scalar relativistic paramagnetic BPPT contribution due to the mass−velocity correction to the reference wave function is enhanced for the confined Xe in the small cavity of C_{60}. Similarly to the Xe···C_6H_6 case, the relativistic shift is sensitive to the percentage of the exact-exchange admixture in the functional and decreases along the BLYP, B3LYP, and BHandHLYP series of methods. Considering the total (NR+BPPT) shift, BHandHLYP gives still a too low value of 139.8 ppm, about 40 ppm below the experimental value. It is worth noting that the B3LYP functional (Table 4) result loses its excellent agreement with the experimental value upon the inclusion of the relativistic shift contribution at the BPPT level, 16.6 ppm. The BPPT relativistic effect that we obtain at the GGA BLYP level, 18.6 ppm, is in excellent agreement with the ZORA data of Autschbach and Zurek using the BP86 functional.[20]

3.3.2. Dynamics of Xe in a Rigid Cage. Energy and Chemical Shift Hypersurfaces. Figure 7 shows the BSSE-corrected SCS-MP2/def-TZVP electronic interaction energy of the Xe atom and the cage (reaction energy of Xe + C_{60} = Xe@C_{60}), where the Xe atom is displaced up to 0.5 Å from the center of the cage along the five distinct symmetry directions toward the cage wall. For details on the directions, see the Computational Methods section. Due to the high symmetry of the cage (I_h), these five directions reveal that the thermally accessible part of the potential energy surface around the center of the cage is, to a good approximation, spherically symmetric. The confinement potential is deep; at 300 K, the displacement of Xe by 0.2, 0.3, and 0.5 Å toward the cage wall corresponds to 3, 7, and 21 times *kT*, respectively. This prevents large-amplitude thermal motion of the Xe atom toward the cage walls.

The calculated potential surface inside of the cage is rather sensitive to basis set effects, as observed in Figure 8. However, for our purposes of modeling the dynamics of the endohedral Xe atom, only the shape of the potential matters. Figure 8 compares the MP2 potentials calculated with different basis sets. (MP2 was performed for this part due to the fact that SCS-MP2 only became available to us in the course of the project.) The shape of the potential is not crucially dependent on the basis set. The method dependence is even smaller than the basis set dependence. Our tests (not shown here) revealed that HF, DFT, and MP2 potentials, to a good approximation, only differ by a certain shift value as compared to the best affordable (SCS-MP2) potential. This is important for the molecular dynamics of the Xe@C_{60} (vide infra), where one can safely employ DFT in first-principles MD simulations of this weakly bonded system, despite the generally poor performance of DFT for absolute energetics.

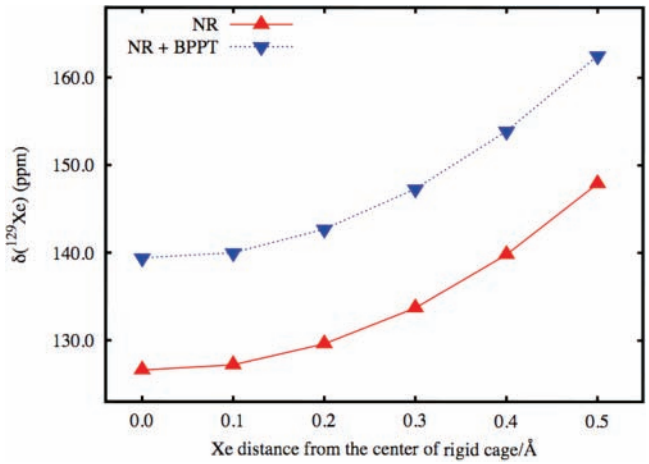

Figure 9. ^{129}Xe chemical shift in Xe@C_{60} for the Xe atom displaced from the center of the C_{60} cage toward the center of a pentagon. The cage is kept rigid. The BHandHLYP functional and the MHA-TZVP basis set were used in the nonrelativistic (NR) calculations. The relativistic BPPT corrections used FIVu61 and def-TZVP basis sets for Xe and C, respectively.

The Xe shift surface in the cage is qualitatively similar to the energetics, as shown in more detail in Table S8 of the Supporting Information. Figure 9 plots results for a single direction toward the center of a pentagon. The demanding BPPT shift surface was only produced along this direction and is also shown in Figure 9. The direction toward a carbon atom was also tested at 0.5 Å from the center, and the difference with the depicted case was found to be negligible. The evolution of the five relevant BPPT terms can be found in Table S9 in the Supporting Information. In the thermally accessible region of Xe at 300 K (<0.15 Å), the curvature of the NR shift surface is quite small and is not changed much by the even flatter relativistic BPPT surface. Only at large distances from the center, close to the fullerene wall, does the steepness of the δ(Xe) surface increase due to relativistic effects, mainly by the

TABLE 6: Temperature Dependence of the ^{129}Xe Chemical Shift Calculated by Solving the Diatomic Rovibrational Problem with the Cage Considered a Rigid Particle and Using the Potential from Figure 7 and Shift from Figure 9[a]

T(K)	δ_{NR}(Xe)	$\delta_{NR+BPPT}$(Xe)[b]
0[c]	126.6	139.4
0	126.8	139.6
50	126.8	139.6
100	126.8	139.6
150	126.9	139.6
200	126.9	139.7
250	127.0	139.8
300	127.1	139.9
350	127.1	140.0
400	127.2	140.0

[a] SCS-MP2/def2-TZVPP is used for the energetics, and BHandHLYP/MHA-TZVP is used for the shifts. [b] Only the five main BPPT terms used. [c] Molecule at rest; no zero-point correction.

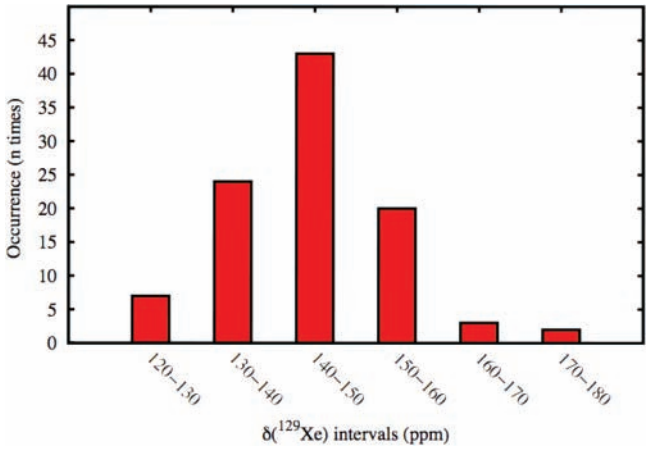

Figure 10. Distribution of the ^{129}Xe shift calculated from snapshots of molecular dynamics trajectories.

most distance-sensitive p/mv contribution. Hence, relativity has an almost constant positive contribution to the Xe shift.

With the endohedral potential and shielding surface spherically symmetric in the region accessible at normal temperatures, we now can consider the Xe atom and the rigid C_{60} cage as two atoms interacting via the SCS-MP2 potential illustrated in Figure 7 and solve the quantum mechanical rovibrational problem accurately.[50] The chemical shift can be averaged using the thermally populated rovibrational states based on its dependence on the Xe displacement (Figure 9). Results of the VIBROT simulations in Table 6 suggest only a very small correction due to the Xe dynamics in the rigid cage, as can be expected from the combination of the relatively deep potential well in Figure 7 and the small dependence of the shift on the Xe displacement (Figure 9). The zero-point correction at 0 K adds about 0.2 ppm to δ(Xe). Increasing the temperature to 300 K adds only another 0.3 ppm.

3.3.3. First-Principles Molecular Dynamics of Xe@C_{60}. Snapshots were taken from the trajectories of 20 MD calculations, and Xe chemical shifts were computed at the BHandHLYP/SVP level. Table S10 in the Supporting Information gives details on which particular snapshots were selected. We are interested in the dynamic contribution (simulation average minus the equilibrium value), which renders the effects related to the basis set to be largely canceled out. Using 5 snapshots from each of the 20 simulations, the dynamically averaged value for δ(Xe) is 145.3 $\pm$ 1.0 ppm, which is 12.8 $\pm$ 1.0 ppm above the BHandHLYP/SVP value for the BP86/SVP-optimized equilibrium geometry. While the effect of Xe dynamics in a rigid cage was found to be a very modest one, the influence of the cage dynamics is in the same direction (increased shift) but much larger. The sign and magnitude of the dynamic contribution are similar to those of the relativistic effect. The distribution of the values is shown in Figure 10. It roughly corresponds to a Gaussian shape. The dynamically corrected relativistic value based on BHandHLYP calculations is 152.6 ppm, still 27 ppm below the experimental value.

The dynamic effect on the ^{13}C shifts can also be extracted from the snapshot calculations. With the data averaged from 100 snapshots of 20 simulations, we obtain a dynamic effect of $+1.4 \pm 0.1$ ppm on the ^{13}C shift when comparing to that of the static BHandHLYP/SVP calculation of the BP86/SVP-optimized Xe@C_{60}. Heine et al. report a dynamic effect of 2.5 ppm for the ^{13}C shift in the empty C_{60} (ref 56). Experimentally, the ^{13}C shift increases by 0.95 ppm upon insertion of Xe into C_{60}, from 143.5 in C_{60} to 144.5 ppm in Xe@C_{60}.[21] Our static BHandHLYP/TZVP calculations result in a corresponding difference between the two situations of 2.2 ppm. It remains to be seen in a future study whether the inclusion of the dynamics of the empty cage at the same level of theory improves the present static results.

3.3.4. Solvent Effects. In ref 20, Autschbach and Zurek estimated the benzene solvent effect to be about 10.0 ppm in the Xe shift using a partial PCM implementation in ZORA, without solvent effects in the response part of the calculation. We were not able to reproduce this result using PCM at the NR level. Only a contribution of nearly +0.3 ppm was obtained using BHandHLYP, even if the geometrical structure of Xe@C_{60} was reoptimized with CPCM and the solvent model was also included in the response part of the shielding calculation. Electrostatic multipole contributions are very small for systems of nearly spherical symmetry.

Solvent effects present a peculiar problem in the present case of Xe@C_{60} in benzene. It is hard to judge a priori whether the effect of solvent shall be large or small as benzene is a weakly bonding solvent of low permittivity but an aromatic system at the same time. The Xe atom is hidden inside of the cage and can be expected to be insensitive to direct interactions with the cage surroundings. On the other hand, the pronounced sensitivity of the Xe chemical shift to both the static cage structure and the dynamics suggests that the solvent may have a substantial indirect effect on δ(Xe). Thus, it is not clear how much of the missing ~27 ppm in the meticulous calculations of this paper arises due to solvent effects.

To gain further understanding, a model with one explicit solvent molecule, that is, the Xe@C_{60}···C_6H_6 system, was designed. In this model, the benzene was either parallel or perpendicular to a hexagon of the C_{60} cage. The structure was optimized, and the Xe shift was calculated. No strong conclusions can be drawn, however, as the calculated changes in δ(Xe) due to the single solvent molecule are about −0.9 ppm for benzene in the parallel orientation and +1.1 ppm in the perpendicular orientation. Modeling of the explicit solvent for the present case is a very challenging problem on its own and must be postponed to future studies. Nevertheless, it appears evident that the present gap between theory and experiment can hardly be entirely due to the presence of solvent effects in the latter. Instead, the deficiencies of even the best-performing present exchange−correlation functional, BHandHLYP, remains the most likely reason for the error.

3.4. Summing up the Contributions and Estimations of Errors. The missing ~+27 ppm in the calculated (NR+BPPT+

dynamics) versus experimental result can be due to several reasons. Solvent effects may influence both in the static picture as well as via the dynamics of the cage, which, in turn, has a marked effect on the Xe shift. There are remaining errors in the NR, relativistic, and dynamics contributions, amounting to up to a few ppm each but most likely not reaching a total effect of 27 ppm.

4. Conclusions

We have calculated the ^{129}Xe chemical shift in Xe@C_{60}, aiming at a systematic inclusion of all physical effects to model the real experimental conditions. Relativistic effects, electron correlation, temperature-dependent dynamics, and solvent effects have been treated using different approximations. The Xe$\cdots$ C_6H_6 model was used to calibrate density functional approaches necessary for the target system. The calibration against correlated ab initio methods indicated that the amount of the exact-exchange admixture in the DFT functional plays an important role in the resulting Xe shift. The BHandHLYP functional performed best both for the shift and shielding anisotropy.

Static quantum chemical calculations on Xe@C_{60} at the equilibrium geometry show a large sensitivity of the Xe shift to the structure used in the shift calculations. Also, the choice of both the exchange and correlation functionals has substantial effects on the result. Relativistic effects were found to be important as they represent an increase of about 10% on top of the static nonrelativistic result.

We further show that due to the deep confining potential in the cage, the contribution from the Xe dynamics inside of a rigid cage is rather negligible (0.5 ppm), and most of the dynamics effect on shift arises from the thermal motion of the cage. Considering that the dynamics and relativity amount together to about 20% (ca. 26 ppm) of the nonrelativistic result, the previously reported nonrelativistic B3LYP data for a static structure are seen to match the experimental result rather by coincidence and must be taken with caution; the inclusion of dynamics and relativity is necessary, and their effects are numerically very significant. Solvent effects were found to be very small at a nonrelativistic level using the CPCM model, $\sim$0.3 ppm. Inclusion of explicit solvent was attempted, but no definite conclusions can be drawn. Explicit solvent effects are postponed for futures studies.

Our best result for the Xe chemical shift in Xe@C_{60} consisting of BHandHLYP static calculations, BPPT relativistic contributions, molecular dynamics of the endohedral complex, and long-range electrostatic solvent effects is 152.9 ppm, still quite far from the experimental value of 179.2 ppm. While this may still be partially attributed to the missing explicit, static, or dynamic solvent effects, the most likely reason is the insufficient performance of the calibrated exchange$-$correlation functional.

Acknowledgment. We acknowledge fruitful discussions with Dage Sundholm (Helsinki) and Jochen Autschbach (Buffalo). The project was supported by a Marie Curie Intra-European Fellowships within the 6th European Community framework Program. The authors are with the Finnish Center of Excellence in Computational Molecular Science. P.L. is an Academy Research Fellow of the Academy of Finland. Both the Academy of Finland and the Emil Aaltonen Foundation are gratefully acknowledged for further financial support. The Magnus Ehrnrooth Foundation is gratefully acknowledged for travel support of M.S. Computational resources were partially provided by CSC Scientific Computing Ltd., Espoo, Finland.

Supporting Information Available: Table S1 provides HF results of the basis set study for Xe$\cdots$$C_6H_6$. Tables S2$-$S5 show numerical data for Figures 2$-$4 and for shielding anisotropy in Xe$\cdots$$C_6H_6$ (Table S3). Tables S6 and S7 show the relativistic BPPT results for Xe$\cdots$$C_6H_6$ in more detail. Tables S8 and S9 give the details for Figure 9. Table S10 lists the snapshots used in the molecular dynamics calculations of the Xe and C chemical shift. This material is available free of charge via the Internet at http://pubs.acs.org.

References and Notes

(1) Gerken, M.; Schrobilgen, G. *Coord. Chem. Rev.* **2000**, *197*, 335.
(2) Jokisaari, J. *Prog. Nucl. Magn. Reson. Spectrosc.* **1994**, *26*, 1, and references therein.
(3) Jokisaari, J. In *NMR of Ordered Liquids*; Burnell, E. E., de Lange C. A., Eds.; Kluwer: Morwell, MA, 2003; pp 109$-$135.
(4) Raftery, D.; Chmelka, B. F. *NMR: Basic Princ. Prog.* **1994**, *30*, 111.
(5) Ratcliffe, C. I. *Annu. Rep. NMR Spectrosc.* **1998**, *36*, 123.
(6) Moudrakovski, I.; Sanchez, A.; Ratcliffe, C. I.; Ripmeester, J. *J. Phys. Chem. B* **2004**, *104*, 7306.
(7) Nagasaka, B.; Omi, H.; Eguchi, T.; Nakayama, H.; Nakamura, N. *Chem. Phys. Lett.* **2001**, *340*, 473.
(8) Schoenborn, B. C.; Watson, H. C.; Kendrew, J. C. *Nature* **1965**, *207*, 28.
(9) Swanson, S. D.; Rosen, M. S.; Coulter, K. P.; Welsh, R. C.; Chupp, T. E. *Magn. Reson. Med.* **1999**, *42*, 1137.
(10) Wolber, J.; Cherubini, A.; Leach, M. O.; Bifone, A. *Magn. Reson. Med.* **2001**, *43*, 491.
(11) Kantola, J.-H.; Vaara, J.; Rantala, T. T.; Jokisaari, J. *J. Chem. Phys.* **1997**, *107*, 6470.
(12) Hanni, M.; Lantto, P.; Iliaš, M.; Jensen, H. J. Aa.; Vaara, J *J. Chem. Phys.* **2007**, *127*, 164313.
(13) Hanni, M.; Lantto, P.; Runeberg, N.; Jokisaari, J.; Vaara, J. *J. Chem. Phys.* **2004**, *121*, 5908.
(14) Bagno, A.; Saielli, G. *Chem.$-$Eur. J.* **2003**, *9*, 1486.
(15) (a) Jameson, C. J.; de Dios, A. C. *J. Chem. Phys.* **1992**, *97*, 417. (b) Jameson, C. J.; Jameson, A. K.; Baello, B. I.; Lim, H. *J. Chem. Phys.* **1994**, *100*, 5965. (c) Jameson, C. J.; Sears, D. N.; de Dios, A. C. *J. Chem. Phys.* **2003**, *118*, 2575. (d) Sears, D. N.; Jameson, C. J. *J. Chem. Phys.* **2003**, *119*, 12231.
(16) Sears, D. N.; Wasylishen, R. E.; Ueda, T. *J. Phys. Chem.* B **2006**, *110*, 11120.
(17) Lintuvuori, J.; Straka, M.; Vaara, J. *Phys. Rev. E* **2007**, *75*, 31707.
(18) Bühl, M.; Patchkovskii, S.; Thiel, W. *Chem. Phys. Lett.* **1997**, *275*, 14.
(19) Sears, D. N.; Jameson, C. J. *J. Chem. Phys.* **2003**, *118*, 9987.
(20) Autschbach, J.; Zurek, E. *J. Phys. Chem.* A **2003**, *107*, 4967.
(21) Syamala, M. S.; Cross, R. J.; Saunders, M. *J. Am. Chem. Soc.* **2002**, *124*, 6216.
(22) (a) Adrian, F. J. *J. Chem. Phys.* **2004**, *120*, 8469. (b) Jameson, C. J.; Sears, D. N.; Murad, S. *J. Chem. Phys.* **2004**, *121*, 9581.
(23) Straka, M.; Vaara, J. *J. Phys. Chem. A* **2006**, *110*, 12338.
(24) Lantto, P.; Vaara, J. *J. Chem. Phys.* **2007**, *127*, 084312.
(25) Straka, M.; Lantto, P.; Räsänen, M.; Vaara, J. *J. Chem. Phys.* **2007**, *127*, 234314.
(26) Vaara, J.; Manninen, P.; Lantto, P.; In *Calculation of NMR and EPR Parameters: Theory and Applications*; Kaupp, M., Bühl, M., Malkin V. G., Eds.; Wiley-VCH: Weinheim, Germany, 2004; pp 209$-$226.
(27) (a) Manninen, P.; Lantto, P.; Vaara, J.; Ruud, K. *J. Chem. Phys.* **2003**, *119*, 2623. (b) Manninen, P.; Ruud, K.; Lantto, P.; Vaara J. *J. Chem. Phys.* **2005**, *122*, 114107. (c) Manninen, P.; Ruud, K.; Lantto, P.; Vaara J. *J. Chem. Phys.* **2006**, *124*, 149901(E).
(28) (a) Barone, V.; Cossi, M. *J. Phys. Chem. A* **1998**, *102*, 1995. (b) Miertus, A.; Scrocco, E.; Tomasi, J. *Chem. Phys.* **1981**, *55*, 117. (c) Cammi, R.; Tomasi, J. *J. Comput. Chem.* **1995**, *16*, 1449. (d) Tomasi, J.; Persico, M. *Chem. Rev.* **2004**, *94*, 2027. (e) CPCM is based on the COSMO model: Klamt, A.; Schürman, G. *J. Chem. Soc.: Perkins Trans.* **1993**, *2*, 799.
(29) Electronic Structure Calculations on Workstation Computers: The Program System TURBOMOLE: Ahlrichs, R.; Bär, M.; Häser, M.; Horn, H.; Kölmel, C. *Chem. Phys. Lett.* **1989**, *162*, 165.
(30) Frisch, M. J.; Trucks, G. W.; Schlegel, H. B.; Scuseria, G. E.; Robb, M. A.; Cheeseman, J. R.; Montgomery, J. A., Jr.; Vreven, T.; Kudin, K. N.; Burant, J. C.; Millam, J. M.; Iyengar, S. S.; Tomasi, J.; Barone, V.; Mennucci, B.; Cossi, M.; Scalmani, G.; Rega, N.; Petersson, G. A.; Nakatsuji, H.; Hada, M.; Ehara, M.; Toyota, K.; Fukuda, R.; Hasegawa, J.; Ishida, M.; Nakajima, T.; Honda, Y.; Kitao, O.; Nakai, H.; Klene, M.; Li, X.; Knox, J. E.; Hratchian, H. P.; Cross, J. B.; Bakken, V.; Adamo, C.; Jaramillo, J.; Gomperts, R.; Stratmann, R. E.; Yazyev, O.; Austin, A. J.; Cammi, R.; Pomelli, C.; Ochterski, J. W.; Ayala, P. Y.; Morokuma, K.; Voth, G. A.; Salvador, P.; Dannenberg, J. J.; Zakrzewski, V. G.; Dapprich, S.; Daniels, A. D.; Strain, M. C.; Farkas, O.; Malick, D. K.; Rabuck, A.

D.; Raghavachari, K.; Foresman, J. B.; Ortiz, J. V.; Cui, Q.; Baboul, A. G.; Clifford, S.; Cioslowski, J.; Stefanov, B. B.; Liu, G.; Liashenko, A.; Piskorz, P.; Komaromi, I.; Martin, R. L.; Fox, D. J.; Keith, T.; Al-Laham, M. A.; Peng, C. Y.; Nanayakkara, A.; Challacombe, M.; Gill, P. M. W.; Johnson, B.; Chen, W.; Wong, M. W.; Gonzalez, C.; Pople, J. A. *Gaussian 03*, revision C.02; Gaussian, Inc.: Wallingford, CT, 2004.

(31) Stanton, J. F.; Gauss, J.; Watts, J. D.; Szalay, P. G.; Bartlett, R. J. with contributions from Auer, A. A.; Bernholdt, D. B.; Christiansen, O.; Harding, M. E.; Heckert, M.; Heun, O.; Huber, C.; Jonsson, D.; Jusélius, J.; Lauderdale, W. J.; Metzroth, T.; Michauk, C.; Price, D. R.; Ruud, K.; Schiffmann, F.; Tajti, A.; Varner, M. E.; Vázquez, J. The integral packages: *MOLECULE* (Almlöf J.; Taylor P. R.), *PROPS* (Taylor P. R.), and *ABACUS* (Helgaker, T.; Jensen, H. J. Aa.; Jørgensen, P.; Olsen J.). See also Stanton, J. F.; Gauss, J.; Watts, J. D.; Lauderdale, W. J.; Bartlett, *R. Int. J. Quantum Chem. Symp.* **1992**, *26*, 879. For current version, see http://www.aces2.de.

(32) *DALTON, a molecular electronic structure program*, release 2.0; 2005; see http://www.kjemi.uio.no/software/dalton/dalton.html.

(33) Becke, A. D. *J. Chem. Phys.* **1993**, *98*, 5648.

(34) Lee, C.; Yang, W.; Parr, R. *Phys. Rev. B* **1998**, *37*, 785.

(35) Becke, A. D. *Phys. Rev. A* **1988**, *38*, 3098.

(36) Perdew, J. P. *Phys. Rev. B* **1986**, *33*, 8822.

(37) Grimme, S. *Chem. Phys.* **2003**, *118*, 9095.

(38) Hedberg, K.; Hedberg, L.; Bethune, D. S.; Brown, C. A.; Dorn, H. C.; Johnson, D. R.; de Vries, M. *Science* **1991**, *254*, 410.

(39) (a) Perdew, J. P.; Burke, K.; Ernzerhof, M. *Phys. Rev. Lett.* **1996**, *77*, 3865. (b) Perdew, J. P.; Burke, K.; Ernzerhof, M. *Phys. Rev. Lett.* **1997**, *78*, 1386(E).

(40) Keal, T. W.; Tozer, D. J. *J. Chem. Phys.* **2003**, *119*, 3015.

(41) Stephens, P. J.; Devlin, F. J.; Chabalowski, C. F.; Frisch, M. J. *J. Phys. Chem.* **1994**, *98*, 11623.

(42) Perdew, J. P.; Chevary, J. A.; Vosko, S. H.; Jackson, K. A.; Pederson, M. R.; Singh, D. J.; Fiolhais, C. *Phys. Rev. B* **1992**, *46*, 6671.

(43) Hamprecht, F. A.; Cohen, A. J.; Tozer, D. J.; Handy, N. C. *J. Chem. Phys.* **1998**, *109*, 6264.

(44) Keal, T. W.; Tozer, D. J. *J. Chem. Phys.* **2004**, *121*, 5654.

(45) (a) Schäfer, A.; Horn, H.; Ahlrichs, R. *J. Chem. Phys.* **1992**, *97*, 2571. (b) Schäfer, A.; Huber, C.; Ahlrichs, R. *J. Chem. Phys.* **1994**, *100*, 5829. (c) Eichkorn, K.; Weigend, F.; Treutler, O.; Ahlrichs, R. *Theor. Chem. Acc.* **1997**, *97*, 119. (d) Weigend, F.; Häser, M.; Patzelt, H.; Ahlrichs, R. *Chem. Phys. Lett.* **1998**, *294*, 143. (e) Weigend, F.; Ahlrichs, R. *Phys. Chem. Chem. Phys.* **2005**, *7*, 3297.

(46) Weigend, F.; Häser, M. *Theor. Chem. Acc.* **1997**, *97*, 331.

(47) Nicklass, A.; Dolg, M.; Stoll, H.; Preuss, H. *J. Chem. Phys.* **1995**, *102*, 8942.

(48) Peterson, K. A.; Figgen, D.; Goll, E.; Stoll, H.; Dolg, M. *J. Chem. Phys.* **2003**, *119*, 11113.

(49) Fægri, K., Jr.; Almlöf, J. *J. Comput. Chem.* **1986**, *7*, 396. See also http://folk.uio.no/knutf/bases/one.

(50) Sundholm, D.; Gauss, J.; Schäfer, A. *J. Chem. Phys.* **1996**, *105*, 11051.

(51) Allen, M. P.; Tildesley, D. J. *Computer Simulations of Liquids*; Oxford University Press: Oxford, U.K., 1987.

(52) Bug, A. L. R.; Wilson, A.; Voth, G. A. *J. Phys. Chem.* **1992**, *96*, 7864.

(53) Flyvbjerg, H.; Petersen, H. G. *J. Chem. Phys.* **1989**, *91*, 461.

(54) Pyykkö, P. *Mol. Phys.* **2001**, *99*, 1617.

(55) Pyykkö, P.; Wang, C.; Straka, M.; Vaara, J. *Phys. Chem. Chem. Phys.* **2007**, *9*, 2954.

(56) Heine, T.; Vietze, K.; Seifert, G. *Magn. Reson. Chem.* **2004**, *42*, S199.

(57) Adamo, C.; Barone, V. *J. Chem. Phys.* **1999**, *110*, 6158.

(58) Staroverov, V. N.; Scuseria, G. E.; Tao, J.; Perdew, J. P. *J. Chem. Phys.* **2003**, *119*, 12129.